Nano Research

Open Access

Research Article

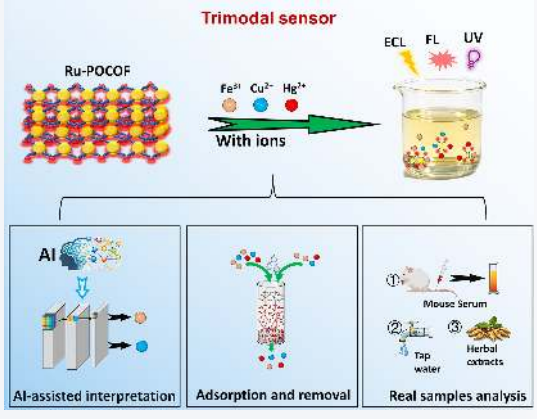
A "trinity" polyoxometalate-functionalized covalent organic framework (Ru-POCOF) for intelligent heavy metal ions sensing

Quan Chen[1], Mei Wang[2], Cheng Zhang[3], Jing Zhang[1], Guobing Wei[1], Fusheng Liao[1], Zhibiao Li[1], Zubin Zhong[1], Huijie Li[1] ✉, Hongjin Lv[4] ✉, and Hao Fan[1] ✉

[1] *Department of Pharmacy, JiangXi University of Chinese Medicine, Nanchang 330004, China*
[2] *Department of Pharmacology, Gannan Health Vocational College, Ganzhou 341000, China*
[3] *Department of GCP, The First Affiliated Hospital, Jiangxi Medical College, Nanchang University, Nanchang 330039, China*
[4] *MOE Key Laboratory of Cluster Science, School of Chemistry and Chemical Engineering, Beijing Institute of Technology, Beijing 102488, China*

Cite this article: *Nano Research*, **2026**, *19*, 94908935. https://doi.org/10.26599/NR.2026.94908935

ABSTRACT: Heavy metal ions pose persistent threats to environmental safety and public health, creating an urgent demand for analytical platforms capable of sensitive, reliable, and visual detection. Herein, a polyoxometalate-functionalized covalent organic framework composite (Ru-POCOF) is developed as a trimodal sensing platform integrating fluorescence (FL), ultraviolet–visible (UV–Vis) absorption, and electrochemiluminescence (ECL) for the detection of Cu^{2+}, Fe^{3+}, and Hg^{2+}. In this architecture, the Ru-COOH ($Ru[dcbpy]_3^{2+}$) complex serves as the photoelectrochemical signal center, while aminated Dawson-type P_2W_{18} clusters are incorporated into an ordered COF scaffold, providing abundant coordination sites and efficient charge-transfer pathways. Benefiting from this synergistic structure, Ru-POCOF exhibits distinct ion-dependent responses across multiple channels: Cu^{2+} and Fe^{3+} induce significant quenching of FL and UV signals accompanied by visible luminescence changes under UV irradiation, whereas Hg^{2+} is sensitively detected through ECL attenuation. Furthermore, machine learning-assisted analysis of spectral features enables accurate discrimination between Fe^{3+} and Cu^{2+}, significantly enhancing analytical reliability in complex matrices. In addition to sensing capability, Ru-POCOF demonstrates rapid adsorption toward Fe^{3+} with a removal efficiency exceeding 60% within 20 min. Reliable detection is validated in tap water, rat serum, and Codonopsis pilosula extracts. Overall, this multifunctional polyoxometalate (POM)–COF hybrid integrates multimodal sensing, visual detection, intelligent analysis, and efficient adsorption, providing a versatile strategy for monitoring trace heavy metal ions in complex systems.



KEYWORDS: polyoxometalates (POMs), polyoxometalate-functionalized covalent organic framework composite (Ru-POCOF), machine learning, heavy metal ions

1 Introduction

Heavy metal ions, such as Cu^{2+}, Fe^{3+}, and Hg^{2+}, are widespread in environmental and biological systems, and their excessive accumulation poses serious threats to ecosystems and human health [1]. Cu^{2+} and Fe^{3+} participate in redox reactions, inducing oxidative stress and cellular damage [2]. In contrast, Hg^{2+} shows pronounced biological toxicity and readily binds thiol-containing proteins and DNA, causing nervous and immune dysfunction [3]. Therefore, developing highly sensitive and selective platforms for heavy metal ion detection is of great significance for environmental monitoring and biomedical applications.

At present, a variety of analytical techniques, including atomic absorption spectroscopy (AAS) [4, 5], inductively coupled plasma mass spectrometry (ICP–MS) [6, 7], and high-performance liquid chromatography (HPLC) [8]. Although these techniques are well established and highly reliable, their broader use in rapid or on-site analysis may still be limited by matrix effects, instrument requirements, operational complexity, and sample pretreatment

Received: April 16, 2026; **Revised:** May 23, 2026
Accepted: June 15, 2026

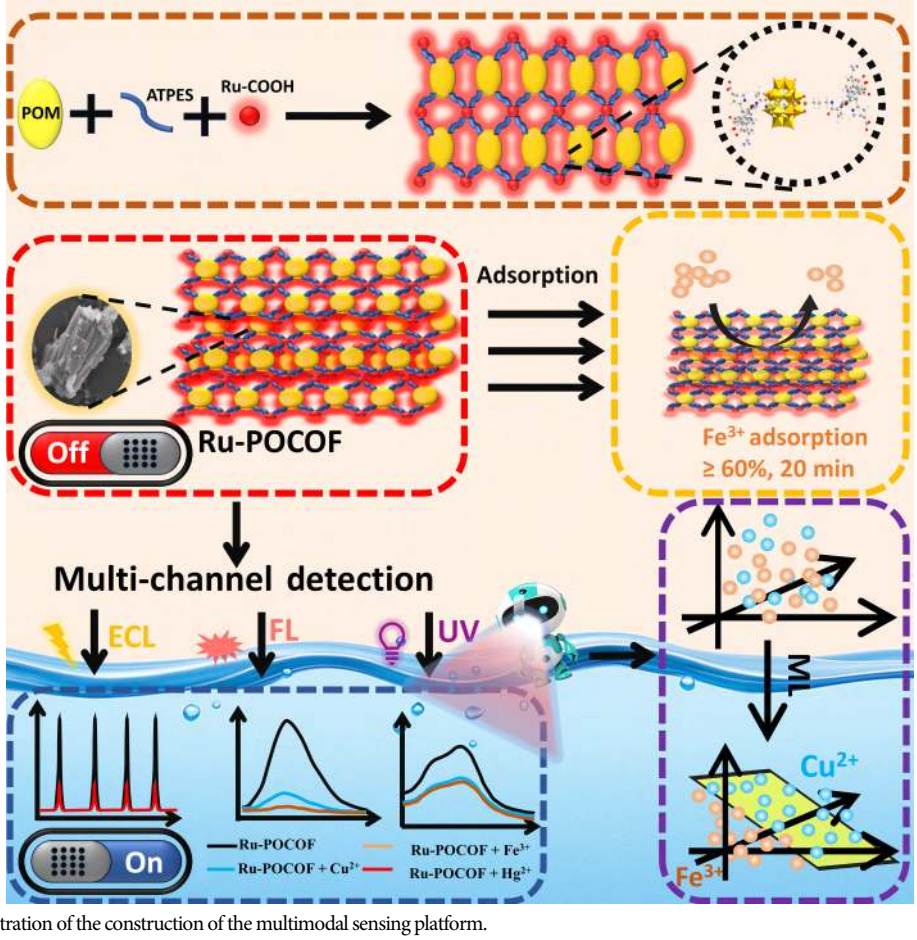
✉Address correspondence to Huijie Li, lihuijie0820@163.com; Hongjin Lv, hlv@bit.edu.cn; Hao Fan, fanhao11@aliyun.com

procedures [9, 10]. Among these methods, luminescence-based sensing strategies have attracted increasing attention for their rapid response, high sensitivity, and operational simplicity [11]. In particular, fluorescence detection offers high sensitivity and intuitive optical readout for rapid analyte monitoring [12]. Electrochemiluminescence, by contrast, provides low background interference, a high signal-to-noise ratio, and controllable electrochemical excitation [13]. In addition, ultraviolet–visible (UV–Vis) absorption signals enable direct visual readout through noticeable spectral changes [14]. However, in complex environmental or biological matrices, single-signal sensing systems may still suffer from background noise or matrix effects, compromising detection reliability [15]. Multimodal sensing relies on functional materials that integrate optical and electrochemical signal centers. Hybrid porous materials integrating photoelectroactive metal complexes and functional inorganic clusters into ordered organic frameworks have emerged as promising candidates [16].

Polyoxometalates (POMs) are anionic metal–oxygen clusters composed of high-valence early transition metals (e.g., V^{5+}, Mo^{6+}, and W^{6+}) linked by oxygen bridges [17]. Owing to their unique electronic structures and excellent charge-transfer properties, POMs are widely regarded as efficient electron donors and versatile building blocks [18]. Among them, Dawson-type P_2W_{18} shows high structural stability and tunable functionalization, enabling efficient electron transport in composite systems [19, 20]. POM-based materials have shown strong potential in pollutant removal and sensing. For example, $[Ni(bipy)_2]_2(HPW_{12}O_{40})$ removes rhodamine B and Cr(VI) from water [21]. Likewise, the EuW@EB-TFP system, formed by *in situ* EuW incorporation into a covalent organic framework (COF) matrix, prolonged fluorescence lifetime and enabled sensitive detection of Ag^+ and the hepatocyte biomarker (CG) in environmental and biological samples [22].

COF–POM hybrids are constructed by functionalizing POMs (e.g., amination and carboxylation) and assembling them with organic frameworks or ligands [23]. This strategy affords stable composites with strong electronic coupling and versatile functionalities through precise structural regulation [24]. Among these approaches, 3-aminopropyltriethoxysilane (APTES)-aminated POMs offer notable structural and functional advantages [25]. They improve hybrid-system stability and electronic coupling while reducing POM leaching in aqueous or variable-pH environments, as previously reported [26]. After integration with Ru-COOH, Ru-COOH serves as the photoelectroactive center, whereas P_2W_{18}–NH_2 provides a rigid framework for charge transfer [27]. This synergy stabilizes Ru complex energy levels, optimizes its coordination environment, and suppresses signal attenuation.

On this basis, APTES-functionalized $K_6[\alpha\text{-}P_2W_{18}O_{62}]$ was integrated with Ru-COOH to construct a Ru-POCOF composite for multimodal heavy metal ion detection (Scheme 1). The platform shows sensitive and differential responses to Cu^{2+}, Fe^{3+}, and Hg^{2+} in ECL, FL, and UV channels via coordination with electron-rich Ru-POCOF sites and photoinduced electron transfer (PET) [28]. Machine learning-assisted multimodal feature extraction and pattern recognition further improved detection accuracy and anti-interference capability [29]. The P_2W_{18}–NH_2 clusters not only



Scheme 1 Schematic illustration of the construction of the multimodal sensing platform.

provide abundant oxygen-rich coordination sites but also form a negatively charged framework, while the carboxyl groups from Ru-COOH further facilitate Fe^{3+} capture through chelation and electrostatic attraction. This dual-site synergistic effect significantly enhances the affinity and adsorption capacity toward Fe^{3+}. Despite limited studies on POMs and COFs for heavy metal detection and adsorption, the rational structural design presented in this work highlights the potential of POMs in functional nanomaterials for environmental monitoring and biomedical analysis.

2 Results and discussion

2.1 Structural characterization of Ru-POCOF

As shown in Fig. 1(a), P_2W_{18} was synthesized, amino-functionalized, and coupled with Ru-COOH via amidation to yield Ru-POCOF. As shown in Fig. 1(b) and Figs. S1(a) and S1(b) in the Electronic Supplementary Material (ESM), scanning electron microscopy (SEM) images show a stacked sheet-like morphology with locally ordered rod-like assemblies, indicating high crystallinity and structural regularity. Transmission electron microscopy (TEM) images (Figs. 1(c)–1(e)) further reveal curved nanosheets and localized wrinkled structures, indicating a flexible, intrinsically porous sheet-like architecture favorable for ion diffusion and electron transport. High-resolution TEM (HRTEM) images (Figs. 2(b) and 2(c)) show distinct lattice fringes with an interplanar spacing of approximately 0.288 nm, indicating nanoscale short-range order in Ru-POCOF, likely from ordered P_2W_{18}-related coordination motifs or locally crystalline domains [30]. Energy-dispersive X-ray spectroscopy (EDS) spectra and elemental mapping (Figs. 1(f)–1(l) and Figs. S1(c)–S1(e) in the ESM) show uniform distribution of O, Ru, Si, P, and W throughout the material, while clear W and Ru signals confirm the successful incorporation of P_2W_{18}–NH_2 and Ru-COOH into the composite framework. Trace K likely arises from residual precursors or the functionalization process (Fig. S1(f) in the ESM). Quantitative analysis reveals relatively high C and O contents, further supporting the effective assembly of the ordered COF scaffold with POM functional units (Figs. S1(g) and S1(h) in the ESM).

As shown in Fig. 2(a), Fourier transform infrared (FT-IR) spectra were collected for Ru-POCOF and its precursors, including P_2W_{18}, P_2W_{18}–NH_2, and Ru-COOH. P_2W_{18} exhibits characteristic vibrational bands in the range of 500–1000 cm^{-1}, which are attributed to W–O–W, W=O, and P–O stretching modes, indicating that the Dawson-type polyoxometalate framework is well preserved [31]. After amination, P_2W_{18}–NH_2 shows slight variations in this region, along with the emergence of a W–O–Si vibration band at 1412 cm^{-1}, confirming the successful grafting of APTES. Ru-COOH displays a characteristic C=O stretching vibration of the carboxyl group at 1714 cm^{-1}. In the FT-IR spectrum of Ru-POCOF, both the characteristic POM vibrations and carboxyl signals are retained, while a new amide (–CONH–) band appear at 1650 cm^{-1}, indicating that P_2W_{18}–NH_2 and Ru-COOH are chemically linked rather than physically mixed [32]. X-ray diffraction (XRD) patterns (Fig. 2(d)) reveal that pristine P_2W_{18} possesses good crystallinity, and its main diffraction peaks are largely retained after amination. In contrast, Ru-COOH exhibits broad diffraction features, indicative of a low-crystallinity organic structure. Ru-POCOF displays diffraction features derived from both components, accompanied by further peak broadening, suggesting the formation of an ordered yet reduced-crystallinity hybrid system after multicomponent integration. The selected-area electron diffraction

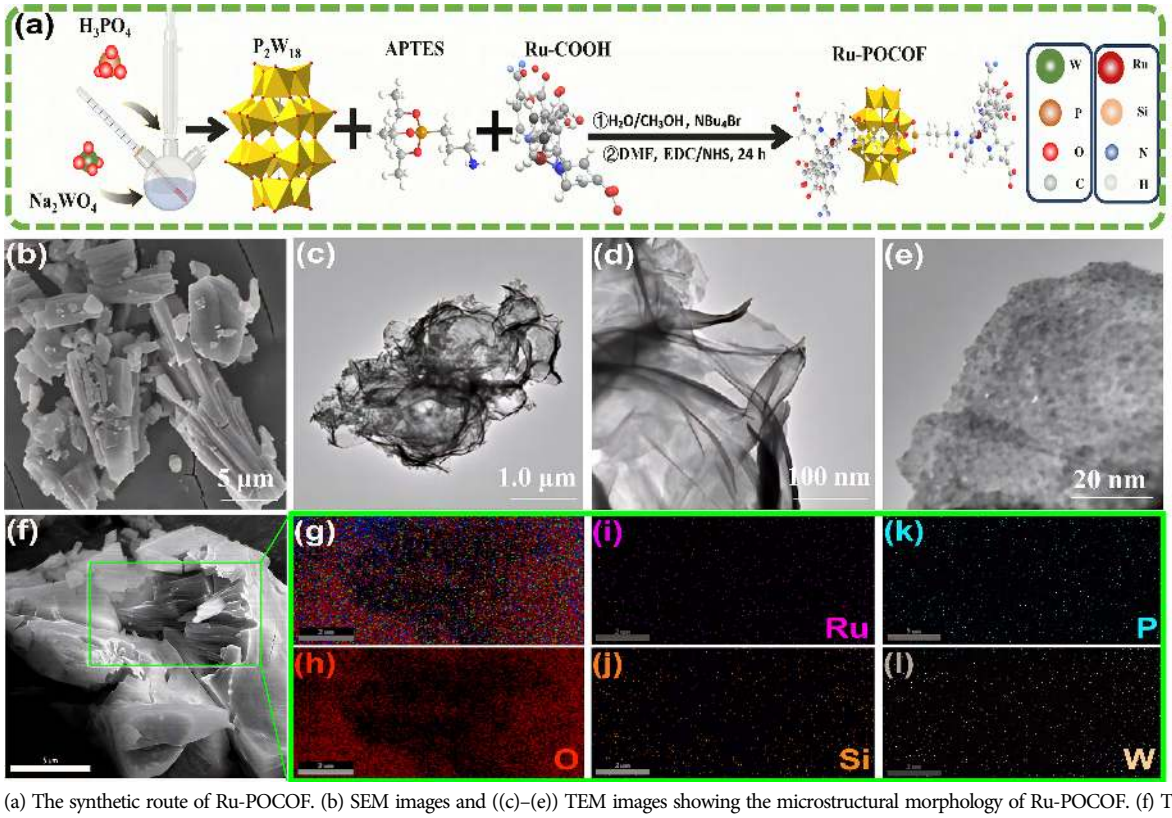


Figure 1 (a) The synthetic route of Ru-POCOF. (b) SEM images and ((c)–(e)) TEM images showing the microstructural morphology of Ru-POCOF. (f) The selected region for EDS analysis. (g) Overall elemental distribution. (h)–(l) Elemental mappings of O, Ru, Si, P, and W.

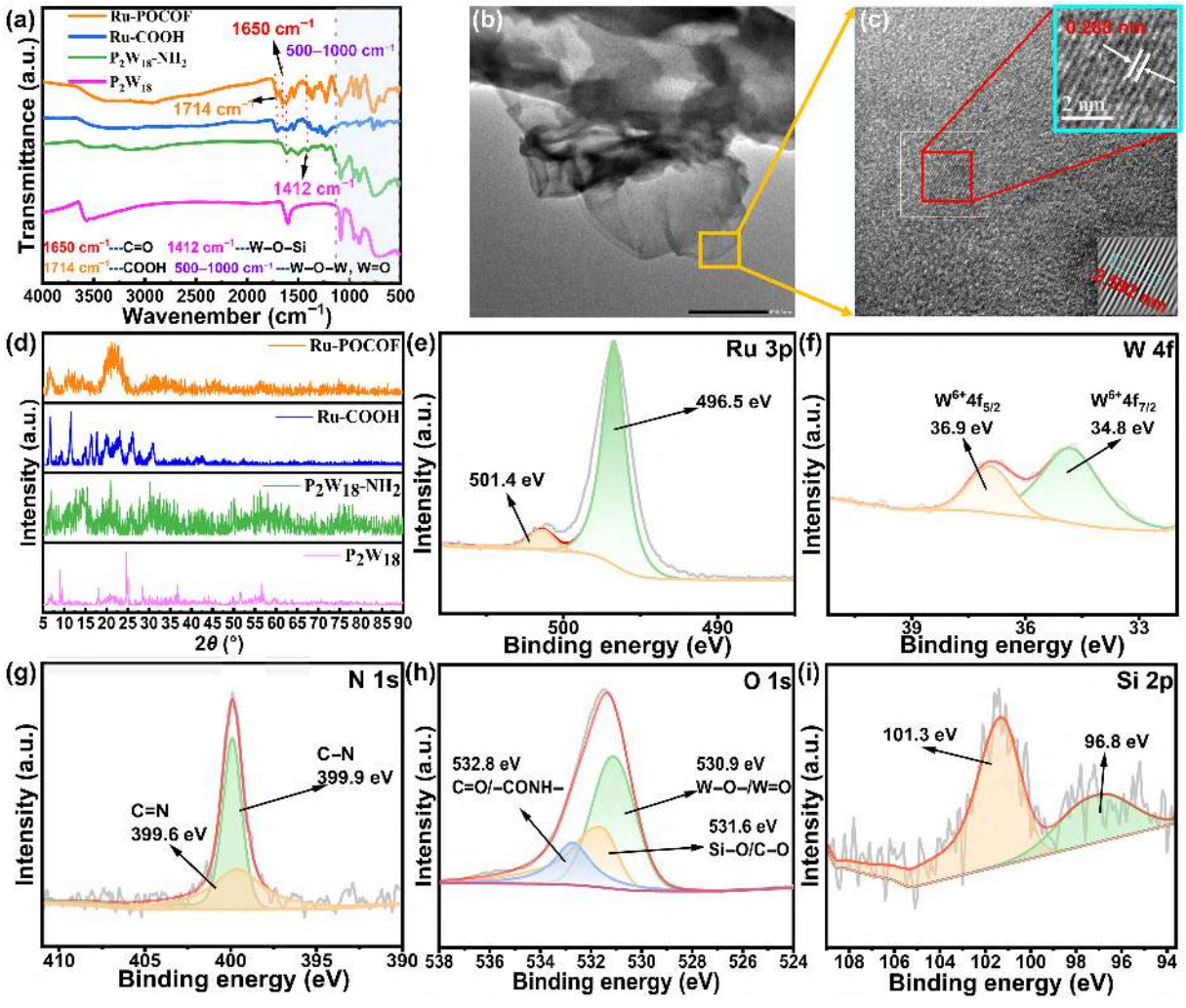


Figure 2 (a) Comparative FT-IR spectra and (d) XRD patterns of Ru-POCOF and its precursors. (b) and (c) HRTEM images of Ru-POCOF. XPS survey spectrum and high-resolution (e) Ru 3p, (f) W 4f, (g) N 1s, (h) O 1s, and (i) Si 2p spectra.

(SAED) pattern (Fig. S2(a) in the ESM) is consistent with the XRD results. X-ray photoelectron spectroscopy (XPS) was employed to investigate the elemental composition and valence states of Ru-POCOF. The survey spectrum clearly reveals the presence of Ru, W, N, P, Si, and K elements (Fig. S2(b) in the ESM). In the high-resolution W 4f spectrum (Fig. 2(f)), the doublet peaks at 35.5 and 37.6 eV are characteristic of W^{6+} species, confirming the preservation of the polyoxometalate structure [33]. The N 1s spectrum (Fig. 2(g)) exhibits peaks at 399.6 and 399.9 eV, which can be assigned to C=N and C–N bonding environments, respectively, indicating the presence of the organic framework and coordination-active sites. The O 1s spectrum (Fig. 2(h)) can be deconvoluted into components corresponding to W–O/W=O, C=O/–CONH–, and Si–O/C–O species, further verifying the coexistence and synergistic integration of POM units and the COF skeleton within a single framework. High-resolution Ru 3p and Si 2p spectra (Figs. 2(e) and 2(i)) further confirm the successful incorporation of Ru-COOH and the effective APTES modification of P_2W_{18}.

2.2 Specificity and stability of Ru-POCOF multi-mode detection

Ru-POCOF exhibits pronounced multimodal responses toward Cu^{2+}, Fe^{3+}, and Hg^{2+} in a homogeneous system, with its luminescence originating from the ^{3}MLCT excited state of the Ru-COOH unit (λ_{abs} = 469 nm, λ_{em} = 632 nm). As shown in Fig. 3(d), under 365 nm UV irradiation, the addition of Fe^{3+} almost completely quenches the solution luminescence, whereas Cu^{2+} induces only weak orange–red emission, and other potential interferents exert negligible effects. In the selectivity experiments, the concentrations of the target ions (Cu^{2+}, Fe^{3+}, and Hg^{2+}) were fixed at 10^{-4} M, while those of other metal ions and biomolecules were set at 10^{-3} M. As illustrated in Figs. 3(b) and 3(c), both Fe^{3+} and Cu^{2+} induce significant decreases in the FL and UV signals, with Fe^{3+} exhibiting a more pronounced quenching effect; detailed UV selectivity spectra are provided in the ESM (Fig. S3(a) in the ESM). In contrast, Hg^{2+} shows only a minor influence on the FL and UV responses but gives rise to pronounced quenching in the ECL channel (Fig. 3(a)). This differential behavior originates from the distinct excitation mechanisms: FL relies predominantly on photoexcitation of the Ru complex, whereas ECL is an electrochemically driven process that is highly sensitive to electron transfer and recombination dynamics [34]. Hg^{2+} possesses a high reduction potential and strong electron-accepting characteristics, enabling coordination with N/O sites in Ru-POCOF and acting as an electron trap to suppress electron–hole recombination, thereby

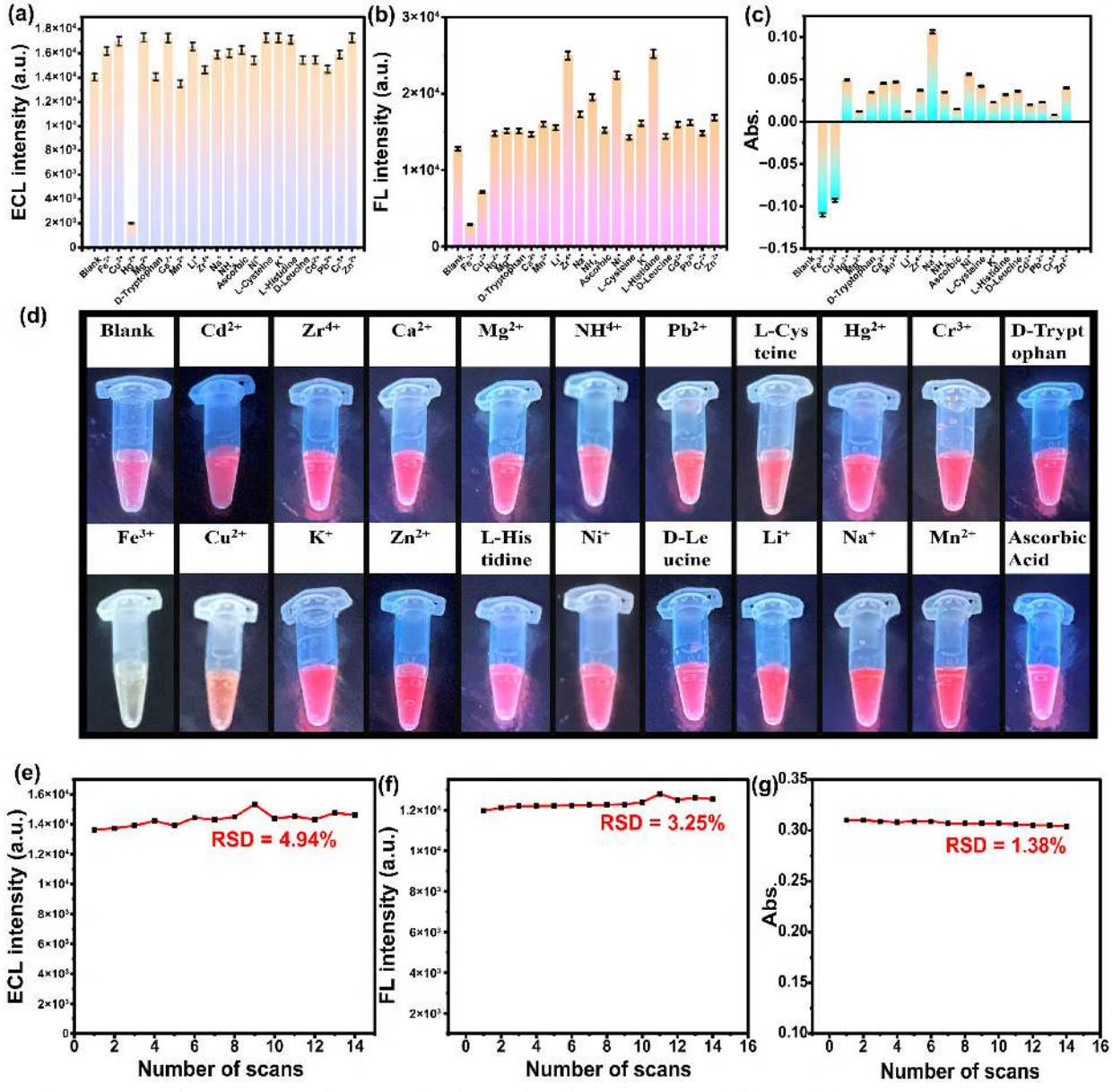


Figure 3 (a) ECL responses of Ru-POCOF toward Hg^{2+} (10^{-4} M) and potential interfering species (10^{-3} M). (b) FL and (c) UV responses to Cu^{2+} and Fe^{3+} (10^{-4} M). (d) Visual luminescence changes under 365 nm UV irradiation; and cyclic stability of (e) FL, (f) UV, and (g) ECL signals over 14 consecutive cycles (n = 14). The concentration of Ru-POCOF was fixed at 0.05 mg·mL^{-1} in all experiments.

leading to a pronounced decrease in ECL intensity [35]. This behavior is consistent with previously reported $Ru(bpy)_3^{2+}$/TSC-based ECL systems [36]. Stability tests demonstrate that Ru-POCOF maintains stable signals responses over 14 consecutive cyclic scans in the FL, UV, and ECL channels (with an interval of 1 min), yielding RSD of 3.25%, 1.38%, and 4.94%, respectively (Figs. 3(e)–3(g), and Figs. S3(c) and S3(d) in the ESM). The probe also shows excellent stability during long-term storage (Fig. S4 in the ESM). In addition, Ru-POCOF at a concentration of 0.05 mg·mL^{-1} exhibits good dispersion stability in deionized water at pH 7.5, as shown in Fig. S5(e) in the ESM.

2.3 Ru-POCOF's detection performance for Cu^{2+}, Fe^{3+}, and Hg^{2+}

Under optimized conditions (Figs. S5(a)–S5(d) in the ESM), the sensing performance of Ru-POCOF toward Fe^{3+}, Cu^{2+}, and Hg^{2+} was systematically evaluated using three detection channels: FL, UV, and ECL. As shown in Fig. 4(a) and Fig. S6(a) in the ESM, increasing concentrations of Fe^{3+} in the range of 10^{-9}–10^{-4} M lead to a continuous decrease in fluorescence intensity, yielding a linear regression equation of $Y = -1078.644 \lg C + 8508.0483$ ($R^2 = 0.995$). As illustrated in Fig. 4(b) and Fig. S6(b) in the ESM, Cu^{2+} likewise induces pronounced fluorescence quenching over the concentration range of 10^{-7}–10^{-3} M, exhibiting an excellent linear relationship described by $Y = -1381.339 \lg C + 10{,}604.551$ (R^2 = 0.997). In the UV channel, the absorbance decreases linearly with increasing Fe^{3+}/Cu^{2+} concentration (Figs. 4(c) and 4(d)), following the linear equation $Y = -0.0252 \lg C + 0.29062$ ($R^2 = 0.995$) (Fig. S6(c) in the ESM) and $Y = -0.0219 \lg C + 0.29956$ ($R^2 = 0.996$) (Fig. S6(d) in the ESM). The ECL channel displays a highly sensitive response toward Hg^{2+}. As shown in Figs. 5(a) and 5(b), a good

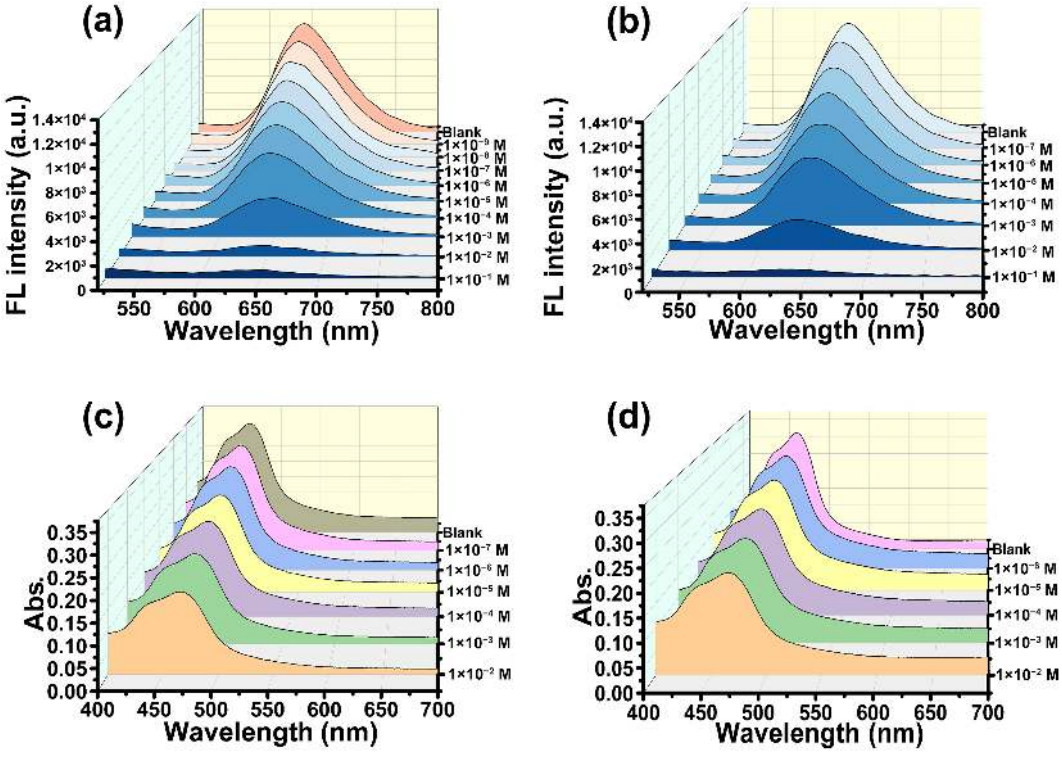


Figure 4 Fluorescence responses of Ru-POCOF to (a) Fe^{3+} and (b) Cu^{2+}. UV–Vis absorption responses to (c) Fe^{3+} and (d) Cu^{2+}.

linear relationship between ECL intensity and Hg^{2+} concentration is observed over the range of 10^{-11}–10^{-4} M, with a regression equation of $Y = -1380.525\lg C + 10{,}463.473$ ($R^2 = 0.996$). Collectively, these results demonstrate that Ru-POCOF enables sensitive and reliable detection of Fe^{3+}, Cu^{2+}, and Hg^{2+} across multiple detection channels, thereby fully highlighting the advantages of this multimodal analytical platform.

By incorporating Ru-COOH as the photoelectrochemical signal center into the Ru-POCOF composite and exploiting the electrostatic attraction and charge-storage capability of POMs, the optical output of the Ru-COOH units is effectively enhanced. Meanwhile, the covalent organic framework architecture improves the dispersion of Ru species and increases the number of accessible coordination sites on the material surface, thereby providing favorable binding sites for heavy metal ions. Owing to these synergistic effects, Ru-POCOF exhibits superior performance in both the detection and adsorption of heavy metal ions, and its advantages compared with representative reported systems are summarized in Table 1.

2.4 ML-assisted identification of Fe^{3+}/Cu^{2+}

Because Fe^{3+} and Cu^{2+} exhibit similar fluorescence quenching behaviors in the Ru-POCOF system, reliable discrimination based solely on spectral intensity variations is challenging. To enhance the discriminative capability of the multimodal sensing platform, ML algorithms were introduced to classify the FL and UV spectral data of Ru-POCOF obtained in the presence of different metal ions. As shown in Fig. 6(a), a binary classification model for Fe^{3+}/Cu^{2+} discrimination was constructed based on a support vector machine (SVM), using spectral features and concentration information as input variables. Through training–testing dataset partitioning and parameter optimization, classification models were independently developed for the FL and UV channels. The results indicate that the areas under the receiver operating characteristic (ROC) curves (AUCs) of the FL and UV models reach 0.9579 and 0.9272, respectively, demonstrating excellent discriminative capability and generalization performance (Figs. 6(c) and 6(g)). The classification confusion matrices (Figs. 6(b) and 6(f)), together with the corresponding performance metrics (Figs. 6(d) and 6(h)), further confirm the robustness and stability of the models. An analysis of classification accuracy across different concentration ranges (Figs. 6(e) and 6(i)) reveals that the models maintain reliable recognition performance over a broad concentration window. The distributions of the original data and statistical box plots of the spectral features are presented in Figs S7(a)–S7(d) in the ESM. Collectively, these results demonstrate that the introduction of machine learning effectively mitigates the influence of signals overlap and background noise on classification outcomes, enabling rapid and accurate discrimination between Fe^{3+} and Cu^{2+} and offering a feasible strategy for identifying complex multi-metal ion systems.

2.5 Exploring the working principle of sensors

Time-resolved fluorescence measurements (Figs. S8(a) and S8(b) in the ESM) further reveal that the fluorescence lifetime of Ru-POCOF is prolonged from 58.85 ns for Ru-COOH to approximately 100 ns, confirming that the incorporation of POM units modulates the coordination environment of the Ru luminophore and effectively suppresses non-radiative decay processes [46–48]. As shown in Figs. S8(c) and S8(d) in the ESM, the introduction of Fe^{3+} and Cu^{2+} leads to simultaneous decreases in the FL and UV signals, indicating the occurrence of a PET process, whereas Hg^{2+} predominantly induces pronounced quenching of the ECL signals (Fig. S8(e) in the ESM).

Notably, Hg and Ru signals exhibit a high degree of spatial overlap (Fig. 7(f)), indicating that Hg^{2+} preferentially interacts in the

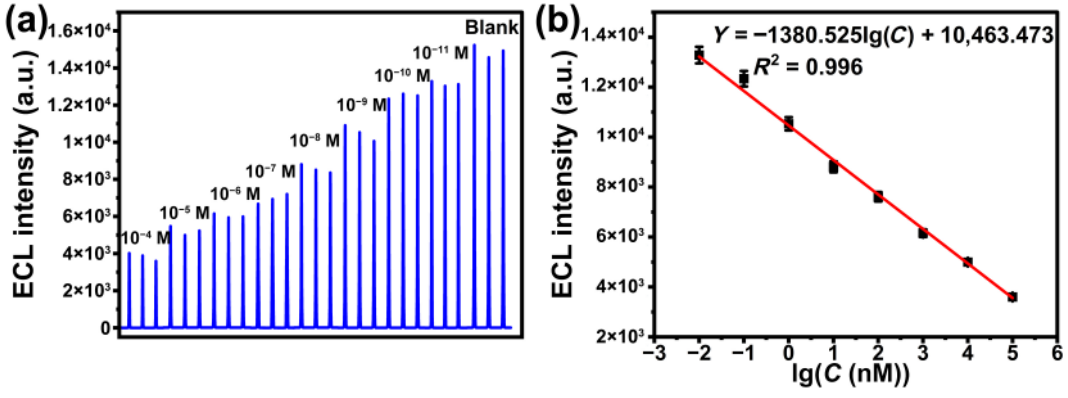


Figure 5 (a) ECL response toward Hg^{2+} together with (b) the corresponding linear relationship.

Table 1 Comparison of various techniques for Cu^{2+}, Fe^{3+}, and Hg^{2+} detection

Analytes	Method	Materials	LOD	Ref.
Cu^{2+}	FL	EXT	0.097 μM	[37]
Cu^{2+}	FL	N2	0.10 μM	[38]
Cu^{2+}	UV	PPDOx	4.14 μM	[39]
Cu^{2+}	FL	Ru-POCOF	0.0607 μM	This work
Cu^{2+}	UV	Ru-POCOF	0.190 μM	This work
Fe^{3+}	FL	CS-TPE	0.998 μM	[40]
Fe^{3+}	FL	PEDOT	0.82 μM	[41]
Fe^{3+}	UV	Cys-caf-AuNP	1.09 μM	[42]
Fe^{3+}	FL	Ru-POCOF	0.318 nM	This work
Fe^{3+}	UV	Ru-POCOF	0.1046 μM	This work
Hg^{2+}	ECL	Mn-3D-C3N4	0.0166 μM	[43]
Hg^{2+}	ECL	MPFS@Ru	0.32 pM	[44]
Hg^{2+}	ECL	RuCOFs	4.17 nM	[45]
Hg^{2+}	ECL	Ru-POCOF	1.17 pM	This work

vicinity of the Ru luminescent centers, which is consistent with its strong ECL quenching effect. XPS analysis further elucidates the underlying electronic structure evolution. In the corresponding XPS survey spectra (Fig. 7(g)), characteristic Fe 2p, Cu 2p, and Hg 4f peaks are observed, further confirming the effective binding of the metal ions. The elemental contents and EDS mapping spectra of the remaining elements are shown in Figs. S9(a)–S9(c) and S9(h)–S9(j) in the ESM. High-resolution XPS analysis shows that the Fe $2p_{3/2}$ and Fe $2p_{1/2}$ peaks appear at 711.83 and 725.03 eV, respectively (Fig. S9(e) in the ESM, which are characteristic of Fe^{3+} species. The Hg $4f_{7/2}$ and Hg $4f_{5/2}$ peaks are located at 100.28 and 104.13 eV, respectively (Fig. S9(f) in the ESM). The Cu $2p_{3/2}$ and Cu $2p_{1/2}$ peaks at 933.63 and 942.78 eV, respectively (Fig. S9(g) in the ESM), are assigned to Cu^{2+} species. These binding energy values are in good agreement with those reported for typical Fe^{3+}, Cu^{2+}, and Hg^{2+}-adsorbed systems in Refs. [49, 50]. In the W 4f region (Fig. 7(h) in the ESM), the main peaks shift toward higher binding energies after interaction with Fe^{3+}, Cu^{2+}, and Hg^{2+}, indicating metal-ion-induced electronic redistribution within the W–O coordination environment of the POM units. Figure S9(d) in the ESM shows that the N 1s binding energy undergoes significant changes under the influence of different metal ions. In Ru-POCOF, the original C=N (~ 399.6 eV) and C–N (~ 399.9 eV) peaks shift upon chelation, indicating that the coordination of metal ions perturbs the N,N-sites on the bipyridine rings and the amino groups introduced by APTES. In the O 1s spectra (Fig. 7(i)), the peaks associated with C=O/–COO^- and W–O species show concurrent shifts, reflecting coordination interactions and electron transfer processes among the metal ions, oxygen-containing groups of the COF, and lattice oxygen of the POM units [51]. Overall, multiple hierarchical coordination sites in Ru-POCOF—including Ru centers, N and O atoms, and POM units—collectively participate in metal ions recognition [52].

To clarify the electronic-structure variations of the system, density functional theory (DFT) calculations of the frontier molecular orbitals (highest occupied molecular orbital (HOMO)/lowest unoccupied molecular orbital (LUMO)) were performed using the DMol³ module in Materials Studio [53]. The exchange-correlation energy was described by the Perdew–Burke–Ernzerhof (PBE) functional within the generalized gradient approximation (GGA) [54, 55], and electron-ion interactions were treated with ultrasoft pseudopotentials using a cutoff energy of 380 eV [56]. Geometry optimization was performed using the Broyden–Fletcher–Goldfarb-Shannon (BFGS) algorithm [57], with convergence thresholds of < 0.001 eV·A^{-1} for Hellmann–Feynman force and 5 × 10^{-5} eV·$atom^{-1}$ for total energy. As shown in Fig. S10 in the ESM, the HOMO and LUMO energy levels display a clear modulation trend from POMs to POMs-NH_2 and then to Ru-POCOF incorporating Ru-COOH. Functionalization shifts the frontier orbitals upward and narrows the energy gap, facilitating electronic transitions. Orbital distribution diagrams further show that Ru-COOH induces tighter coupling between the frontier orbitals and the organic ligand segments [58].

As shown in Figs. 8(a)–8(c), coordination with heavy metal ions markedly alters the electronic distribution and energy-level structure. Heavy metal ion binding rearranges the frontier orbitals, causing electrons to transfer from the original LUMO (–6.125 eV) to a newly formed HOMO and disrupting the original LUMO (–6.125 eV)-to-HOMO (–6.373 eV) transition pathway. The excited electrons are thus redistributed within a new energy-level framework, suppressing the optical signals generated by electronic transitions. This process is attributed to the PET effect (Fig. 8(d)). Specifically, Fe^{3+} and Cu^{2+}, as strong electron acceptors, effectively couple with the electron-rich domains (POMs and N/O sites) in Ru-POCOF, facilitating the transfer of excited-state electrons from Ru-POCOF to the metal ions. This reduces the number of emissive species in the excited state, ultimately resulting in significant signal quenching. In contrast, due to its higher reduction potential (0.92 eV), Hg^{2+} exhibits a stronger coordination affinity toward

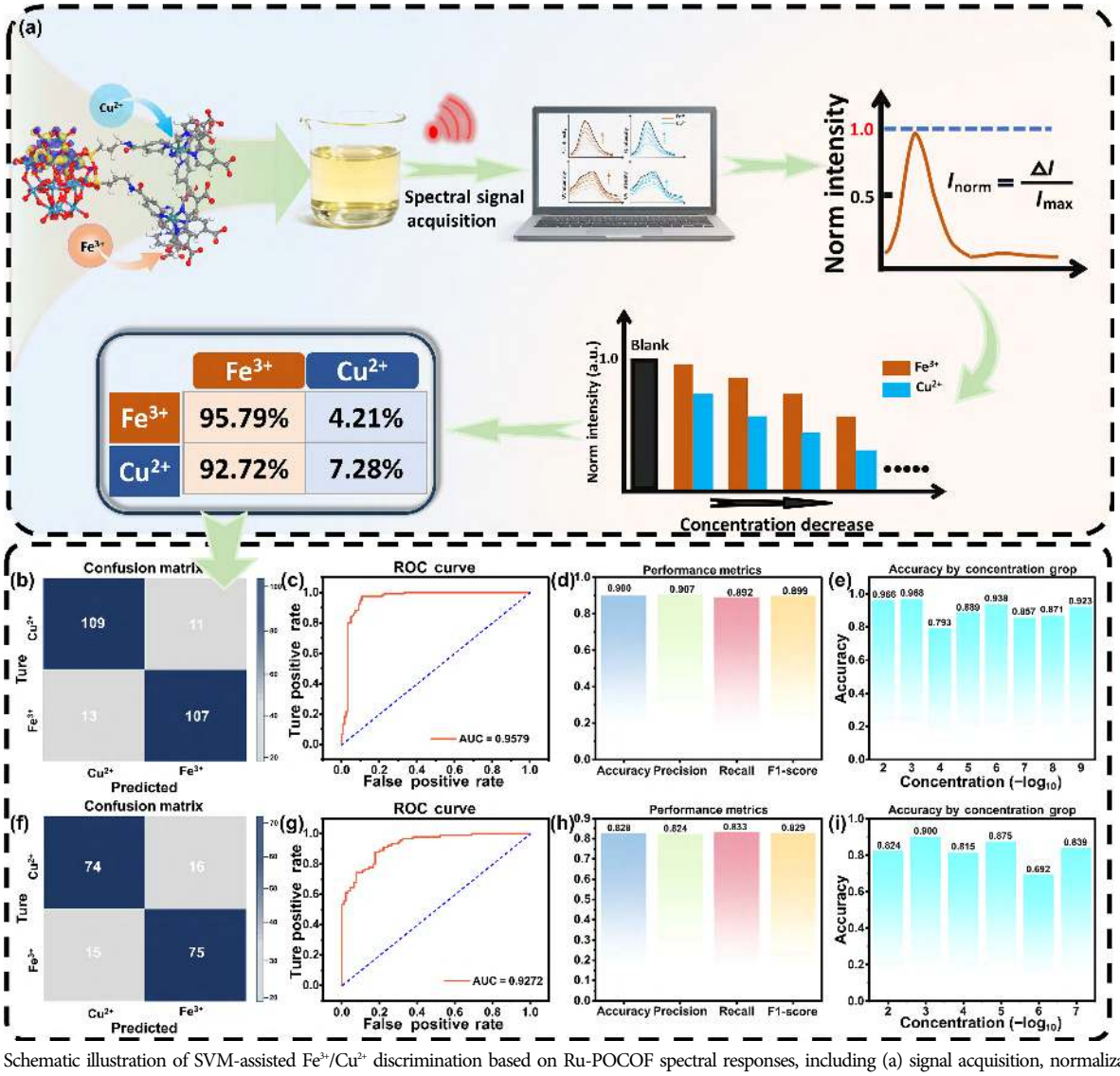


Figure 6 Schematic illustration of SVM-assisted Fe^{3+}/Cu^{2+} discrimination based on Ru-POCOF spectral responses, including (a) signal acquisition, normalization, and model input, (b) and (f) confusion matrices, (c) and (g) ROC curves, (d) and (h) performance metrics, and ((e) and (i)) classification accuracy across different concentration ranges.

electron-rich sites. The resulting stable coordination structure promotes electron dissipation under electrochemical excitation, thereby significantly enhancing the ECL quenching effect. However, during light absorption or spontaneous fluorescence excitation, Hg^{2+} may not significantly perturb the formation or decay pathways of the excited states, leading to negligible changes in UV–Vis absorption and FL signals [59–61].

2.6 Adsorption and removal of Fe^{3+} ions by Ru-POCOF

The adsorption of various heavy metal ions by Ru-POCOF was systematically evaluated by a batch equilibrium method [62]. Ru-POCOF was dispersed in standard solutions of Fe^{3+}, Cu^{2+}, Hg^{2+}, Mn^{2+}, Cr^{3+}, Cd^{2+}, and Pb^{2+} and shaken at 25 °C to equilibrium. After centrifugation, residual metal ions concentrations were measured by inductively coupled plasma mass spectrometry (ICP–MS). The removal efficiency (η), adsorption capacity (q_t), and distribution coefficient (K_d) were calculated from Eqs. (1)–(3). Kinetics were fitted using pseudo-first-order and pseudo-second-order models based on Eqs. (4) and (5), with fitted parameters summarized in Figs. S11(a) and S11(b) and Table S1 in the ESM.

$$q_t = \frac{(C_0 - C_t) \times V}{m} \tag{1}$$

$$\eta = \frac{(C_0 - C_t)}{C_0} \times 100\% \tag{2}$$

$$K_d = \frac{(C_0 - C_t) \times V}{m \times C_t} \tag{3}$$

$$q_{t1} = q_e (1 - e^{-k_1 t}) \tag{4}$$

$$q_{t2} = \frac{k_2 q_e^2 t}{1 + k_2 q_e t} \tag{5}$$

As shown in Figs. S12(a) and S12(b) in the ESM, under coexistence of multiple metal ions, Ru-POCOF preferentially adsorbs Fe^{3+}, with a removal efficiency up to 62%, much higher than

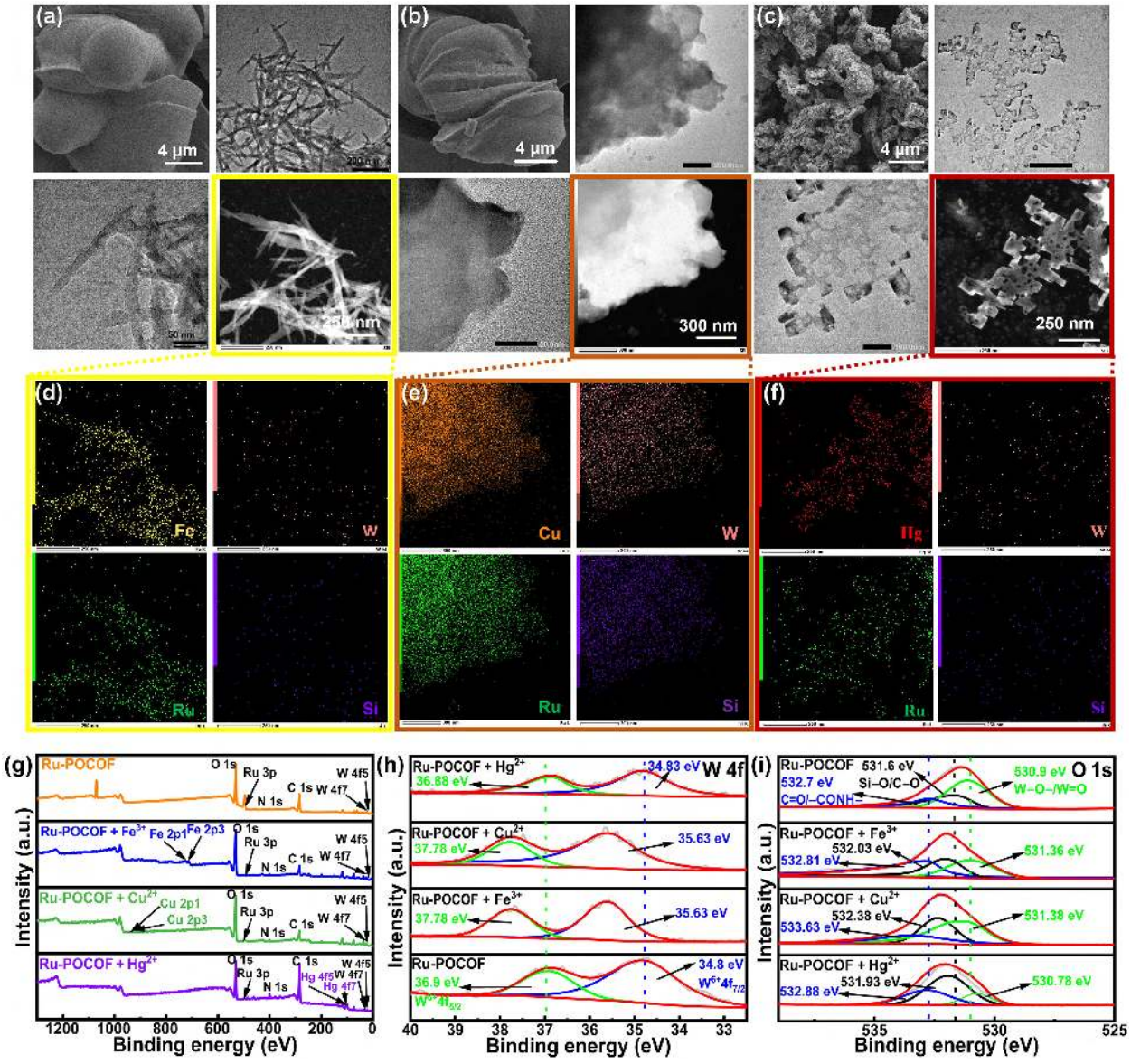


Figure 7 SEM/TEM morphologies and corresponding EDS elemental mappings of Ru-POCOF after interaction with ((a) and (d)) Fe^{3+}, ((b) and (e)) Cu^{2+}, and ((c) and (f)) Hg^{2+}. High-resolution XPS spectra of the corresponding samples, including (g) full spectrum, (h) W 4f, and (i) O 1s.

that for other heavy metal ions (< 30%). Fe^{3+} adsorption kinetics (Fig. S12(c) in the ESM) show rapid uptake to near-equilibrium within 20 min, with an experimental equilibrium capacity of 689.8 mg·g^{-1} (Table S2 in the ESM). The pseudo-second-order model fits the data better (R^2 = 0.9976) than the pseudo-first-order model (R^2 = 0.9904), and gives a calculated q_e of 739.8 mg·g^{-1}, closer to the experimental value (Fig. S12(d) in the ESM). These results indicate chemisorption, consistent with the spectroscopic quenching and coordination mechanism discussed above. The high Fe^{3+} adsorption stems from the negatively charged, oxygen-rich P_2W_{18} units anchored by APTES, which enhance electrostatic attraction and coordination affinity, as well as the ordered COF pore channels with electron-rich N/O sites, which provide a size-matched and stable coordination environment. Owing to its high charge density and small ionic radius, Fe^{3+} therefore outcompetes other metal ions. These results are consistent with recent studies showing that functionalized COF-based materials can serve as efficient platforms for heavy metal ion detection, adsorption, and enrichment. Compared with widely reported COF adsorbents for Hg^{2+}, Pb^{2+}, Cr^{4+}, and U^{4+}, Fe^{3+}-focused COF sensing/adsorption systems remain relatively limited, highlighting the significance of Ru-POCOF as an integrated platform for Fe^{3+} detection, recognition, and enrichment. Representative studies on COF-based heavy metal ion sensing, adsorption, and enrichment are further summarized in Table S3 in the ESM.

2.7 Practical application analysis of Ru-POCOF

To assess the practical applicability of the Ru-POCOF multimodal sensing platform, spike-and-recovery experiments were performed in tap water, rat serum, and Codonopsis pilosula extracts. All samples were filtered through a 0.22 μm membrane before analysis, and rat serum and herbal extracts were diluted prior to use. In tap water spiked with Fe^{3+}, Cu^{2+}, and Hg^{2+}, recoveries ranged from 99.26% to 103.00% with low RSDs (Table S4 in the ESM), indicating high accuracy and reliability. In rat serum spiked with 1, 5, and 25 μM Fe^{3+}, recoveries of 97.20%–106.60% were obtained

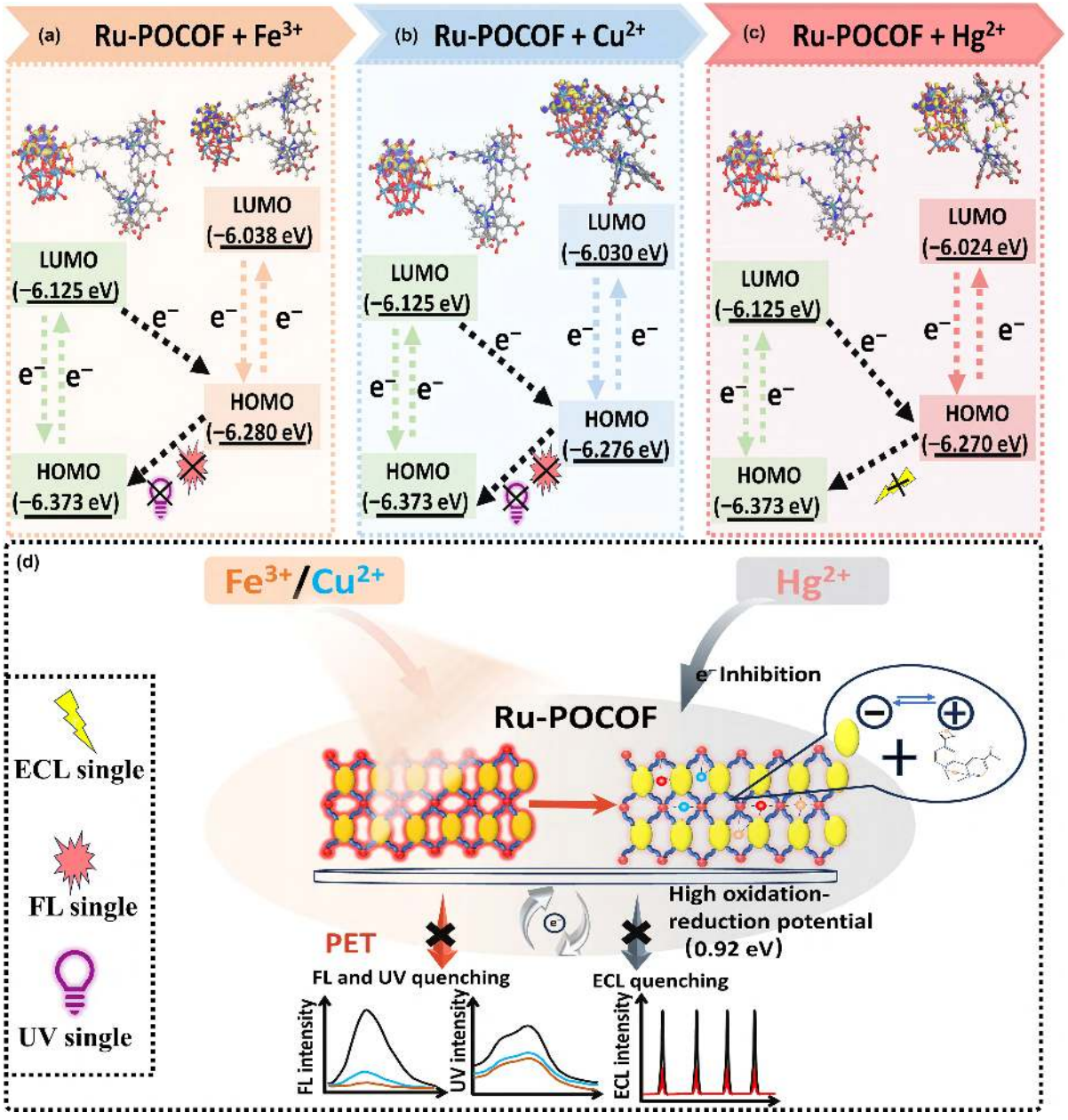


Figure 8 Orbital diagrams of HOMO and LUMO energy levels of Ru-POCOF after interaction with (a) Fe^{3+}, (b) Cu^{2+}, and (c) Hg^{2+}. (d) Schematic illustration of the proposed mechanism.

(Table S5 in the ESM), in good agreement with ICP–MS results, confirming satisfactory performance in biological samples. For Codonopsis pilosula extracts spiked with 5–25 μM $HgCl_2$, recoveries ranged from 95.00% to 104.60%, with RSDs of 0.89%–3.02% (Table S6 in the ESM), demonstrating good robustness in complex herbal matrices. These results confirm that the Ru-POCOF platform possesses excellent accuracy, stability, and anti-interference capability, highlighting its promise for practical applications.

3 Conclusion

In this study, a polyoxometalate–covalent organic framework composite material, Ru-POCOF, functionalized with polyacid P_2W_{18}, was constructed to achieve integrated multimodal detection and adsorption removal of heavy metal ions. Benefiting from the electron-storage capability of P_2W_{18} and the ordered porous framework of the COF, the material exhibited sensitive and distinct responses across ECL, FL, and UV channels, demonstrating excellent selectivity and photoelectronic performance toward Fe^{3+}, Cu^{2+}, and Hg^{2+} ions. The integration of machine learning algorithms significantly enhanced the discrimination accuracy between Fe^{3+} and Cu^{2+}. Meanwhile, Ru-POCOF demonstrated rapid adsorption kinetics and a high removal efficiency (62% within 20 min) for heavy metals, along with excellent stability and reliability in real water samples, biological fluids, and traditional Chinese medicine extracts. In summary, this work proposes a multimodal analytical strategy integrating detection, recognition, and removal functions, offering a novel approach for photoelectronic co-regulation of POM-COF composite systems and their applications in environmental and bioanalytical fields.

Electronic Supplementary Material: Supplementary material is available in the online version of this article at https://doi.org/10.26599/NR.2026.94908935.

Data availability

All data needed to support the conclusions in the paper are presented in the manuscript and the Electronic Supplementary Material. Additional data related to this paper may be requested from the corresponding author upon request.

Acknowledgements

The authors sincerely acknowledge financial support from the following projects: the Science and Technology Innovation Team Development Program of Jiangxi University of Chinese Medicine (No. CXTD22005), the Jiangxi Provincial Key Laboratory of Effective Substances in Traditional Chinese Medicine (No. 2024SSY07102), and the Doctoral Research Initiation Fund of Jiangxi University of Chinese Medicine (No. 2023BSZR024). In addition, this work was further supported by the Jiangxi Provincial Youth Science and Technology Talent Program (No. 20244BCE52050), the Graduate Innovation Special Fund of Jiangxi University of Chinese Medicine (No. XJ-S202507), and the Jiangxi Provincial Graduate Innovation Special Fund (No. YC2025-S717).

Declaration of competing interest

All the contributing authors report no conflict of interests in this work.

Author contribution statement

Q. C.: Methodology, investigation, writing – original draft, data curation, visualization, conceptualization. M. W.: Investigation, resources. C. Z.: Methodology. J. Z.: Resources, investigation. G. B. W.: Methodology, investigation. F. S. L.: Methodology, data curation. Z. B. L.: Data curation. Z. B. Z.: Data curation, investigation. H. J. L.: Funding acquisition, resources, methodology, project administration, supervision, writing – review & editing. H. J. L.: Methodology, investigation. H. F.: Methodology, project administration.

Use of AI statement

None.

References

[1] Fouda, S. H.; El-Halim, E. S. A.; Ghany, H. A. A. Radiological and chemical hazards of persistent organic pollutants in the textile sector. *Sci. Rep.* **2025**, *15*, 20102.

[2] Wei, F.; Meng, Y.; Zhu, D. X.; Wu, J. Mechanism and role of ferroptosis in the development of gastric cancer. *Clin. Exp. Med.* **2025**, *25*, 182.

[3] Aaseth, J.; Ajsuvakova, O. P.; Skalny, A. V.; Skalnaya, M. G.; Tinkov, A. A. Chelator combination as therapeutic strategy in mercury and lead poisonings. *Coord. Chem. Rev.* **2018**, *358*, 1–12.

[4] Arokiasamy, P.; Abdullah, M. M. A. B.; Arifi, E.; Jamil, N. H.; Othuman Mydin, M. A.; Abd Rahim, S. Z.; Sandu, A. V.; Ishak, S. Sustainable geopolymer adsorbents utilizing silica fume as a partial replacement for metakaolin in the removal of copper ion from synthesized copper solution. *Case Stud. Constr. Mater.* **2025**, *22*, e04142.

[5] Tuzen, M.; Soylak, M. Multi-element coprecipitation for separation and enrichment of heavy metal ions for their flame atomic absorption spectrometric determinations. *J. Hazard. Mater.* **2009**, *162*, 724–729.

[6] Mosallaei, S.; Abbasi, S.; Jalalian, E.; Amiri, H.; Hoseini, M. Heavy metals in edible red soil of the rainbow island in the Persian gulf: Concentration and health risk assessment. *Chemosphere* **2023**, *331*, 138778.

[7] Feng, Y. W.; Luo, C.; Yang, Y. S.; Zheng, X. L.; Du, Z. Y.; Yang, Y. B.; Zhou, Z.; Chen, H. B.; Wang, X.; He, J. X. et al. Engineering lanthanide ion-labeled aptamers for ICP-MS profiling of serum-derived extracellular vesicles from colorectal cancer. *JACS Au* **2025**, *5*, 4740–4749.

[8] Dhokpande, S. R.; Deshmukh, S. M.; Khandekar, A.; Sankhe, A. A review outlook on methods for removal of heavy metal ions from wastewater. *Sep. Purif. Technol.* **2024**, *350*, 127868.

[9] Ge, S. B.; Wei, K. X.; Peng, W. X.; Huang, R. Z.; Akinlabi, E.; Xia, H. Y.; Shahzad, M. W.; Zhang, X. H.; Xu, B. B.; Jiang, J. C. A comprehensive review of covalent organic frameworks (COFs) and their derivatives in environmental pollution control. *Chem. Soc. Rev.* **2024**, *53*, 11259–11302.

[10] Liang, Y. M.; Qi, Y.; Zhong, N. N.; Jin, Y. S.; Shao, B. Covalent organic frameworks as advanced materials for adsorption and analysis of contaminants in environmental, biological and food matrices. *Coord. Chem. Rev.* **2025**, *533*, 216507.

[11] Malik, L. A.; Bashir, A.; Qureashi, A.; Pandith, A. H. Detection and removal of heavy metal ions: A review. *Environ. Chem. Lett.* **2019**, *17*, 1495–1521.

[12] Liang, M. J.; Liu, C. Y.; Li, Y. X.; Shi, Q.; Zha, H.; Yang, J. Y.; Deng, Z. H.; Zhang, X. Development and validation of a multi-platform LAMP system for rapid HAdV-3 and HAdV-7 detection. *Eur. J. Clin. Microbiol. Infect. Dis.* **2025**, *44*, 2665–2675.

[13] Zhang, Z.; Liu, J. H.; Dai, Y.; Ye, M. F.; Sun, Y. D.; Zhang, K.; Xu, J. J. Dual-mode SERS-ECL biosensor for robust detection of circulating miRNAs based on *in-situ* synthesized probes. *Chem. Eng. J.* **2024**, *495*, 153607.

[14] Li, J. W.; Yin, C. X.; Liu, T.; Wen, Y.; Huo, F. J. A new mechanism-based fluorescent probe for the detection of ClO^- by UV–vis and fluorescent spectra and its applications. *Sens. Actuators B: Chem.* **2017**, *252*, 1112–1117.

[15] Babamiri, B.; Bahari, D.; Salimi, A. Highly sensitive bioaffinity electrochemiluminescence sensors: Recent advances and future directions. *Biosens. Bioelectron.* **2019**, *142*, 111530.

[16] Gao, P. F.; Liu, Y. X.; Zhang, L. N.; Zhang, S. M.; Li, H. W.; Wu, Y. Q.; Wu, L. X. Cell receptor screening for human papillomavirus invasion by using a polyoxometalate-peptide assembly as a probe. *J. Colloid Interface Sci.* **2018**, *514*, 407–414.

[17] He, D. L.; Jiang, Y. B.; Guillén-Soler, M.; Geary, Z.; Vizcaíno-Anaya, L.; Salley, D.; Gimenez-Lopez, M. D. C.; Long, D. L.; Cronin, L. Algorithm-driven robotic discovery of polyoxometalate-scaffolding metal-organic frameworks. *J. Am. Chem. Soc.* **2024**, *146*, 28952–28960.

[18] Lai, Q. S.; Li, X. X.; Zheng, S. T. All-inorganic POM cages and their assembly: A review. *Coord. Chem. Rev.* **2023**, *482*, 215077.

[19] Boskovic, C. Rare earth polyoxometalates. *Acc. Chem. Res.* **2017**, *50*, 2205–2214.

[20] Granadeiro, C. M.; Julião, D.; Ribeiro, S. O.; Cunha-Silva, L.; Balula, S. S. Recent advances in lanthanide-coordinated polyoxometalates: From structural overview to functional materials. *Coord. Chem. Rev.* **2023**, *476*, 214914.

[21] Li, F.; Chen, Y.; Huang, H. M.; Cao, W.; Li, T. H. Removal of rhodamine B and Cr(VI) from aqueous solutions by a polyoxometalate adsorbent. *Chem. Eng. Res. Des.* **2015**, *100*, 192–202.

[22] Wang, J. M.; Xu, X.; Zhao, L. M.; Yan, B. *In situ* growth of

polyoxometalate in COF for trace monitoring of Ag^+ and hepatocellular carcinoma biomarker via a dual responsive strategy. *J. Mater. Chem. C* **2021**, *9*, 9492–9498.
[23] Xue, R.; Liu, Y. S.; Wang, M. Y.; Guo, H.; Yang, W.; Yang, G. Y. Combination of covalent organic frameworks (COFs) and polyoxometalates (POMs): The preparation strategy and potential application of COF-POM hybrids. *Mater. Horiz.* **2023**, *10*, 4710–4723.
[24] Zhang, J. W.; Huang, Y. C.; Li, G.; Wei, Y. G. Recent advances in alkoxylation chemistry of polyoxometalates: From synthetic strategies, structural overviews to functional applications. *Coord. Chem. Rev.* **2019**, *378*, 395–414.
[25] Li, H. Y.; Zheng, L. R.; Lu, Q. C.; Li, Z.; Wang, X. A monolayer crystalline covalent network of polyoxometalate clusters. *Sci. Adv.* **2023**, *9*, eadi6595.
[26] Kong, H.; Ma, P. T.; Wang, J. P.; Niu, J. Y. Overview of organophosphonate covalently modified polyoxometalates: From synthesis and structural diversity to applications. *Polyoxometalates* **2025**, *4*, 9140103.
[27] Hill, C. L. Introduction: Polyoxometalates-multicomponent molecular vehicles to probe fundamental issues and practical problems. *Chem. Rev.* **1998**, *98*, 1–2.
[28] Li, Y. J.; Chen, M. H.; Han, Y. N.; Feng, Y. Q.; Zhang, Z. J.; Zhang, B. Fabrication of a new corrole-based covalent organic framework as a highly efficient and selective chemosensor for heavy metal ions. *Chem. Mater.* **2020**, *32*, 2532–2540.
[29] Zhang, X.; Zhu, W. W.; Zhang, S. T.; Wang, F. B. Machine learning-driven graphene quantum dot fluorescence array for rapid heavy metal ions detection and identification. *Environ. Res.* **2026**, *290*, 123489.
[30] Anyushin, A. V.; Kondinski, A.; Parac-Vogt, T. N. Hybrid polyoxometalates as post-functionalization platforms: From fundamentals to emerging applications. *Chem. Soc. Rev.* **2020**, *49*, 382–432.
[31] Liu, L. H.; Liu, Y. F.; Zhang, L. Q.; Zhang, M.; Ma, P. T.; Yang, G. P. A heptanuclear zirconium cluster-threaded polyoxotungstate wheel for the catalytic synthesis of benzodiazepines. *Chin. Chem. Lett.*, in press, DOI: 10.1016/j.cclet.2025.111882.
[32] Hussain, Z.; Mahmood, A.; Shah, Q.; Imran, A.; Mughal, E. U.; Khan, W.; Baig, A.; Iqbal, J.; Mumtaz, A. Synthesis and evaluation of amide and thiourea derivatives as carbonic anhydrase (CA) inhibitors. *ACS Omega* **2022**, *7*, 47251–47264.
[33] Parveen, S.; Cochran, E. W.; Zulfiqar, S.; Amin, M. A.; Farooq Warsi, M.; Chaudhary, K. Iron/vanadium co-doped tungsten oxide nanostructures anchored on graphitic carbon nitride sheets (FeV-WO_3@g-C_3N_4) as a cost-effective novel electrode material for advanced supercapacitor applications. *RSC Adv.* **2023**, *13*, 26822–26838.
[34] Wang, X. H.; Zhang, M.; Huo, X. L.; Zhao, W.; Kang, B.; Xu, J. J.; Chen, H. Y. Modulating the electronic structure of a semiconductor to optimize its electrochemiluminescence performance. *Nanoscale Adv.* **2019**, *1*, 1965–1969.
[35] Das, G. S.; Shim, J. P.; Bhatnagar, A.; Tripathi, K. M.; Kim, T. Biomass-derived carbon quantum dots for visible-light-induced photocatalysis and label-free detection of Fe(III) and ascorbic acid. *Sci. Rep.* **2019**, *9*, 15084.
[36] Barkae, T. H.; Yuan, F.; Fereja, T. H.; Kitte, S. A.; Ma, X. G.; Zhang, W.; Xu, G. B. Tris(2,2′-bipyridine)ruthenium(II)/thiosemicarbazide electrochemiluminescence for the detection of thiosemicarbazide and mercury (II). *Electrochim. Acta* **2021**, *380*, 138171.
[37] Shi, J. L.; Liu, Y. Z.; Wu, Y. Q.; Miao, Y. X.; Xin, X. P.; Shen, F. F.; Zhao, L. X.; Cao, D. L.; Li, S. L. A copper-bridged fluorescent sensor for sequential detection of Cu^{2+} and TKX-50: Synthesis, mechanism, and applications. *Anal. Chim. Acta* **2025**, *1377*, 344683.
[38] Bai, Y. J.; Zhang, H. P.; Yang, B. Q.; Leng, X. Development of a fluorescein-based probe with an "off–on" mechanism for selective detection of copper(II) ions and its application in imaging of living cells. *Biosensors (Basel)* **2023**, *13*, 301.
[39] You, Y. J.; Li, D.; Chen, Z. Z.; Zhang, X. N.; Hu, Y. X.; Ouyang, S. G.; Li, N. Fluorescent and colorimetric dual-mode detection of Cu^{2+} based on carbon dots. *Microchim. Acta* **2024**, *191*, 563.
[40] Wang, P. Y.; Lv, Y. P.; Hou, X. H.; Yang, X. L.; Tao, Q.; Li, G. Y. Chitosan based fluorescent probe with AIE property for detection of Fe^{3+} and bacteria. *Int. J. Biol. Macromol.* **2024**, *279*, 135478.
[41] Zhen, D. S.; Zhang, S. Q.; Yang, A. F.; Li, L.; Cai, Q. Y.; Grimes, C. A.; Liu, Y. A PEDOT enhanced covalent organic framework (COF) fluorescent probe for *in vivo* detection and imaging of Fe^{3+}. *Int. J. Biol. Macromol.* **2024**, *259*, 129104.
[42] Borah, N.; Kalita, A. J.; Guha, A. K.; Das, M. R.; Tamuly, C. Highly selective, rapid and simple colorimetric detection of Fe^{3+} in fortified foods by L-Cysteine modified AuNP. *Microchem. J.* **2022**, *179*, 107480.
[43] Xie, F. Q.; Wu, X. R.; Li, J. J.; Lu, S. Y.; Du, X.; Chen, Z. H.; Zhang, Y.; Cao, L. L.; Li, X. W.; Liu, Q. An aptasensor based on variable-valence metal-mediated dual-enhancement ECL strategy for the detection of Hg^{2+} in environmental water samples. *Microchem. J.* **2025**, *216*, 114614.
[44] Ma, Y. D.; Yu, Y. J.; Mu, X. Y.; Yu, C.; Zhou, Y.; Chen, J.; Zheng, S. T.; He, J. L. Enzyme-induced multicolor colorimetric and electrochemiluminescence sensor with a smartphone for visual and selective detection of Hg^{2+}. *J. Hazard. Mater.* **2021**, *415*, 125538.
[45] Hu, H. T.; Yin, Z. J.; Cui, H. F.; Xiong, W.; Yu, F. Y.; Zhang, J.; Liao, F. S.; Wei, G. B.; Yang, L.; Zhang, J. et al. A novel dual-detection electrochemiluminescence sensor for the selective detection of Hg^{2+} and Zn^{2+}: Signal suppression and activation mechanisms. *Anal. Chim. Acta* **2024**, *1330*, 343283.
[46] Chen, J.; Xiong, X. L.; Ye, J. R.; Shuai, X. J.; Zhou, J.; Liu, Q. Q.; Huang, C. Z.; Liu, H. Machine learning-assisted three-dimensional fluorescence for heavy metal multi-sensing. *Sens. Actuators B: Chem.* **2025**, *431*, 137385.
[47] Iwai, R.; Suzuki, S.; Sasaki, S.; Sairi, A. S.; Igawa, K.; Suenobu, T.; Morokuma, K.; Konishi, G. I. Bridged stilbenes: AIEgens designed via a simple strategy to control the non-radiative decay pathway. *Angew. Chem., Int. Ed.* **2020**, *59*, 10566–10573.
[48] Saha, A.; Kundu, S.; Verma, M.; Rajput, S. K.; Butcher, R. J.; Datta, A.; Patra, A. K. Fine-tuning the excited-state dynamics of heteroleptic ruthenium(II) polypyridyl complexes with systematic variation of benzazole-substituted 8-hydroxyquinolines. *Inorg. Chem.* **2025**, *64*, 8906–8922.
[49] Cheng, W. R.; Zhang, H. B.; Luan, D. Y.; Lou, X. W. Exposing unsaturated Cu_1–O_2 sites in nanoscale Cu-MOF for efficient electrocatalytic hydrogen evolution. *Sci. Adv.* **2021**, *7*, eabg2580.
[50] Liu, M. J.; Wang, Z. Y.; Song, Z. Q.; Wang, F. C.; Zhao, G. Y.; Zhu, H. J.; Jia, Z. F.; Guo, Z. B.; Kang, F. Y.; Yang, C. A popcorn-inspired strategy for compounding graphene@$NiFe_2O_4$ flexible films for strong electromagnetic interference shielding and absorption. *Nat. Commun.* **2024**, *15*, 5486.
[51] Wang, Z. H.; Wang, X. F.; Tan, Z.; Song, X. Z. Polyoxometalate/metal-organic framework hybrids and their derivatives for hydrogen and oxygen evolution electrocatalysis. *Mater. Today Energy* **2021**, *19*, 100618.
[52] Saqib, M.; Bashir, S.; Ali, S.; Hao, R. Highly selective and sensitive detection of mercury(II) and dopamine based on the efficient electrochemiluminescence of $Ru(bpy)_3^{2+}$ with acridine orange as a coreactant. *J. Electroanal. Chem.* **2022**, *906*, 115896.
[53] Hu, W.; Qiang, T. T.; Li, C. C.; Ren, L. F.; Cheng, F.; Wang, B. S.; Li, M. L.; Song, X. J.; James, T. D. Imaging of hypochlorous acid in mitochondria using an asymmetric near-infrared fluorescent probe with large Stokes shift. *Chem. Sci.* **2022**, *13*, 11140–11149.
[54] Hasnip, P. J.; Pickard, C. J. Electronic energy minimisation with ultrasoft pseudopotentials. *Comput. Phys. Commun.* **2006**, *174*, 24–29.
[55] Perdew, J. P.; Chevary, J. A.; Vosko, S. H.; Jackson, K. A.; Pederson,

M. R.; Singh, D. J.; Fiolhais, C. Atoms, molecules, solids, and surfaces: Applications of the generalized gradient approximation for exchange and correlation. *Phys. Rev. B* **1992**, *46*, 6671–6687.

[56] Vanderbilt, D. Soft self-consistent pseudopotentials in a generalized eigenvalue formalism. *Phys. Rev. B* **1990**, *41*, 7892–7895.

[57] Jiang, J. J.; Ying, S. W.; Wu, C. X.; Yang, C. Enhancing electrical conductivity in zirconium-doped SiC ceramics through synergistic effects of crystal structure and free carbon control. *RSC Adv.* **2024**, *14*, 34328–34337.

[58] Cao, Y. D.; Hans, S.; Liese, J.; Werner-Zwanziger, U.; Wang, J.; Bennett, J. C.; Dunlap, R. A.; Obrovac, M. N. $Si(CO)_y$ negative electrodes for Li-ion batteries. *Chem. Mater.* **2021**, *33*, 7386–7395.

[59] Li, J. Y.; Wang, L. D.; Zhao, Z. F.; Sun, B. X.; Zhan, G.; Liu, H. Y.; Bian, Z. Q.; Liu, Z. W. Highly efficient and air-stable Eu(II)-containing azacryptates ready for organic light-emitting diodes. *Nat. Commun.* **2020**, *11*, 5218.

[60] Kaviani, S.; Shahab, S.; Sheikhi, M.; Ahmadianarog, M. DFT study on the selective complexation of meso-2,3-dimercaptosuccinic acid with toxic metal ions (Cd^{2+}, Hg^{2+} and Pb^{2+}) for pharmaceutical and biological applications. *J. Mol. Struct.* **2019**, *1176*, 901–907.

[61] Liu, Y.; Liu, C. Y.; Zhang, Z. Y. Synthesis of highly luminescent graphitized carbon dots and the application in the Hg^{2+} detection. *Appl. Surf. Sci.* **2012**, *263*, 481–485.

[62] Mei, Y. C.; Zhuang, S. T.; Wang, J. L. Adsorption of heavy metals by biochar in aqueous solution: A review. *Sci. Total Environ.* **2025**, *968*, 178898.

This is an open access article under the terms of the Creative Commons Attribution 4.0 International License (CC BY 4.0, https://creativecommons.org/licenses/by/4.0/).

© The Author(s) 2026. Published by Tsinghua University Press.